Article

Single-Scan NMR Spectroscopy at Arbitrary Dimensions

Yoav Shrot, and Lucio Frydman

J. Am. Chem. Soc., **2003**, 125 (37), 11385-11396• DOI: 10.1021/ja0350785 • Publication Date (Web): 19 August 2003

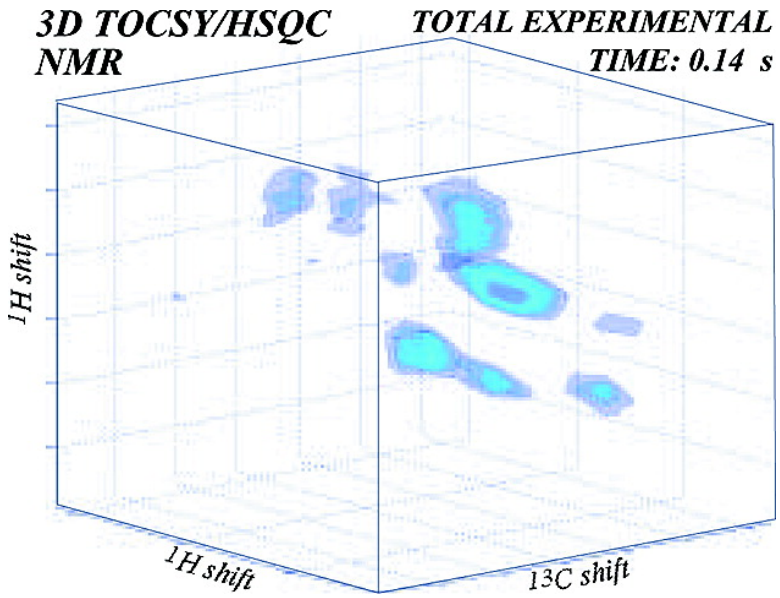

More About This Article

Additional resources and features associated with this article are available within the HTML version:

- Supporting Information
- Links to the 5 articles that cite this article, as of the time of this article download
- Access to high resolution figures
- Links to articles and content related to this article
- Copyright permission to reproduce figures and/or text from this article

View the Full Text HTML

J|A|C|S
ARTICLES
Published on Web 08/19/2003

Single-Scan NMR Spectroscopy at Arbitrary Dimensions

Yoav Shrot and Lucio Frydman*

Contribution from the Department of Chemical Physics, Weizmann Institute of Science, 76100 Rehovot, Israel

Received March 10, 2003; E-mail: lucio.frydman@weizmann.ac.il

Abstract: Multidimensional nuclear magnetic resonance (NMR) provides one of the foremost analytical tools available to elucidate the structure and dynamics of complex molecules in their native states. Executing this kind of experiment generally requires collecting an *n*-dimensional time-domain signal *S*, from which the spectrum arises via an appropriate Fourier analysis of its various time variables. This time-domain signal is actually measured directly only along one of the time axes, while the effects introduced by the remaining time variables are monitored via a parametric incrementation of their values throughout independent experiments. Two-dimensional (2D) NMR experiments thus usually require longer acquisition times than unidimensional experiments, 3D NMR is orders-of-magnitude more time consuming than 2D spectroscopy, etc. Very recently, we proposed and demonstrated an approach whereby data acquisition in 2D NMR can be parallelized, enabling the collection of complete 2D spectral sets within a single transient. The present paper discusses the extension of this 2D NMR methodology to an arbitrary number of dimensions. The principles of the ensuing ultrafast *n*-dimensional NMR approach are described, and a variety of homo- and heteronuclear 3D and 4D NMR spectra collected within a fraction of a second are presented.

Introduction

Few spectroscopic techniques match the role that nuclear magnetic resonance (NMR) plays in contemporary science.[1−7] This position of preeminence was made possible by numerous discoveries and improvements that transformed NMR from the basic analytical tool it was 50 years ago, to one capable of unraveling in vivo metabolism and in vitro structures approaching the megadalton limit.[8,9] Two important landmarks along this development were the advent of pulsed Fourier transform (FT) NMR and of multidimensional NMR spectroscopy.[10−13] The first of these methodologies enabled the eventual extension of NMR to nuclei other than protons, while the second expanded NMR's scope beyond the analysis of simple molecules and into the realm of complex chemical and biological systems. The marked improvements that in terms of resolution and information are furnished by such multidimensional NMR experiments do, however, come at a price. Indeed, even when dealing with systems where the signal-to-noise ratio (S/N) is not a limiting obstacle, the acquisition times of multidimensional NMR tend to be longer than those of their one-dimensional counterparts. This is a consequence of the manner by which the spin evolution within the time-domain is monitored during the course of these experiments: according to the canonical acquisition scheme of multidimensional NMR, the actual physical signal induced by nuclear spins on the pick-up coil is directly measured solely along one of the time axes, while the spins' evolution along the remaining axes is indirectly monitored via a stepwise incrementation of their associated time parameters throughout the sequence. Given that tens or hundreds of data points are usually required along any of the time axes for properly characterizing the internal evolution frequencies, and that each point along the indirect time-domains becomes associated with an independent signal acquisition, extended experimental times become a built-in feature of multidimensional NMR.

Very recently, we have demonstrated an alternative route for collecting 2D NMR spectra whereby the usual time encoding along the indirect domain is replaced by an equivalent encoding of the spin evolution along a spatial axis.[14,15] This spatial encoding is a procedure that unlike the serial incrementation of t_1 values hitherto used in 2D NMR can be parallelized, making

(1) *Encyclopedia of NMR*; Grant, D. M., Harris, R. K., Eds.; J. Wiley & Sons: Chichester, 1996.
(2) Wuthrich, K. *NMR of Proteins and Nucleic Acids*; J. Wiley & Sons: New York, 1986.
(3) Ernst, R. R.; Bodenhausen, G.; Wokaun, A. *Principles of Nuclear Magnetic Resonance in One and Two Dimensions*; Clarendon: Oxford, 1987.
(4) Schmidt-Rohr, K.; Spiess, H. W. *Multidimensional Solid-State NMR and Polymers*; Academic Press: London, 1994.
(5) Sanders, J. K. M.; Hunter, B. K. *Modern NMR Spectroscopy: A Guide for Chemists*; Oxford University Press: Oxford, 1994.
(6) Cavanagh, J.; Fairbrother, W. J.; Palmer, A. G., III; Skelton, N. J. *Protein NMR Spectroscopy: Principles and Practice*; Academic Press: San Diego, 1996.
(7) Brown, M. A.; Semelka, R. C. *MRI: Basic Principles and Applications*; Wiley-Liss: New York, 1999.
(8) Emsley, J. W.; Feeney J. *Prog. Nucl. Magn. Reson. Spectrosc.* **1995**, *28*, 1.
(9) Fiaux, J.; Bertelsen, E. B.; Horwich, A. L.; Wuthrich, K. *Nature* **2002**, *418*, 207.
(10) Lowe, I. *Phys. Rev. Lett.* **1959**, *2*, 285.
(11) Ernst, R. R.; Anderson, W. *Rev. Sci. Instrum.* **1966**, *37*, 93.
(12) Jeener, J. Ampere International Summer School II, Basko Polje, Yugoslavia, September, 1971.
(13) Aue, W. P.; Bartholdi, E.; Ernst, R. R. *J. Chem. Phys.* **1976**, *64*, 2229.
(14) Frydman, L.; Scherf, T.; Lupulescu, A. *Proc. Natl. Acad. Sci. U.S.A.* **2002**, *99*, 15858.
(15) Frydman, L.; Scherf, T.; Lupulescu, A. *J. Am. Chem. Soc.* **2003**, *125*, 9204.

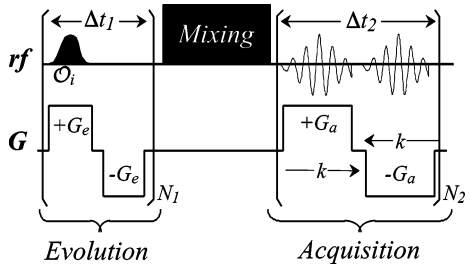

Figure 1. Basic sequence involved in the collection of 2D NMR spectra within a single-scan. A train of N_1 frequency-shifted pulses $\{O_i\}_{1\le i\le N_1}$ is applied in the presence of an oscillating field gradient G_e to achieve the sequential excitation of spins throughout different positions in the sample. Following an arbitrary mixing sequence, data are collected while in the presence of an oscillating acquisition gradient G_a, which enables one to monitor in a spatially resolved fashion the behavior of the spins at different spatial positions. Acquisition of the signal as a function of (k,t_2), followed by its FT along t_2, enables one to retrieve a complete 2D NMR spectrum within a single scan.

it possible to collect the equivalent of complete $S(t_1,t_2)$ data sets within a single scan. The purpose of this Article is to describe how such a methodology can be extended to encompass what could in principle amount to an arbitrary number of spectral dimensions. Toward this end, we begin by reviewing ultrafast NMR as it applies to the 2D case, assuming as in the past that its spatial encoding is implemented with the aid of a linear magnetic field gradient. We then proceed to demonstrate that no specific gradient geometry is actually required to spatially encode single-scan 2D NMR data, as the same goal can be achieved with the aid of magnetic fields possessing nearly arbitrary spatial dependencies. This is an important point, as it serves as the basis for extending the spatial encoding principles that we have so far demonstrated on 2D NMR to include an additional dimension. It is shown that combinations of linearly independent gradient geometries can be used to simultaneously monitor the spins' evolution along separate time axes; a variety of homo- and heteronuclear examples of the ensuing 3D single-scan NMR methodology incorporating both *z*- and *x*-field gradients is then presented. We conclude by deriving an extension of these single-scan principles to accommodate an arbitrary number of spectral dimensions and present as examples of these concepts a series of 4D NMR spectra, each of which were collected within acquisition times under 0.1 s.

Spatial Encoding and the Acquisition of 2D NMR Data in a Single Scan

The basic pulse sequence that we have proposed for the collection of 2D NMR spectra within a single scan is shown in Figure 1 and can be summarized by the scheme

$$\underset{\text{preparation/excitation}}{\text{spatially selective}} - \underset{\text{evolution } (t_1)}{\text{position-dependent}} - \underset{\text{mixing}}{\text{position-independent}} - \underset{\text{acquisition } (t_2)}{\text{spatially resolved}} \quad (1)$$

It is easiest to envision the main features imparted by this sequence if one assumes that the sample under analysis is homogeneous and that the spatially selective excitation it requires is achieved via the application of a magnetic field gradient $G = \partial B_o/\partial r$. The excitation portion of the approach involves a train of N_1 spatially selective rf pulses, which have been spread at constant frequency intervals $\Delta O = |O_{i+1} - O_i|$ and are applied at equal time increments Δt_1. Spins excited by such an rf pulse train will undergo a sequential excitation and thus accumulate an overall internal evolution phase that will depend on their spatial positions within the sample. Magnetizations will also accumulate an extra position-dependent encoding arising from the application of the gradient that is used to achieve the spatial-selective excitation. Such imaging information, however, is undesired in the current spectroscopic context, and ends up being eliminated by a reversal in the gradient carried out in synchrony with the selective rf excitations. The situation of the spins at the conclusion of the t_1 evolution period is thus as illustrated on the left-side panel of Figure 2: nuclear magnetizations (or more generally, spin coherences) will have evolved into a discrete "winding" of N_1 spin-packets, whose pitch solely reflects the internal evolution frequencies Ω_1 that were active during the evolution. Deriving a qualitative description of the basic features of this helix of spin-packets is relatively straightforward. Because the sample is assumed homogeneous, the individual amplitude $A(r)$ of each spin-packet will be simply proportional to the sample volume that it originates from. As for the phases evolved by these individual spin-packets, these will be given by the usual $\Omega_1 t_1$ factor. The proportionality that the frequency-shifted excitation pulses create between evolution time t_1 and the coordinates r allows one to rewrite such phase encoding as $C\Omega_1(r - r^o)$, where r^o and $C = \Delta t_1/\Delta r = \Delta t_1/[\Delta O/\gamma_e G_e]$ are constants depending on the excitation details of the experiment. When taken in unison, these arguments lead to an overall sample magnetization M that at the conclusion of the evolution period is given by

$$M(N_1\Delta t_1) = \sum_r A \cdot e^{iC\Omega_1(r - r^o)} \quad (2)$$

If considered for arbitrary Ω_1 values, this equation, once summed over all coordinates in the sample, predicts that no macroscopic signal will be detectable at the end of the t_1 evolution period.

This initial encoding of the pulse sequence is followed by a generic mixing period, which being coherent in nature will preserve the phases acquired by spin-packets at the conclusion of their t_1 evolution times. Therefore, as the mixing period ends, no signal will be observable from the helical distribution into which the magnetization had been originally wound up. Signal digitization, however, begins while in the presence of an acquisition gradient G_a. The overall purpose of this gradient is to enable a spatially resolved acquisition of the NMR signal, a goal which can only be achieved if G_a's spatial dependence is identical to that of the gradient used during the course of the initial excitation. Because of this dependence, spin-packets at different locations will accrue additional spatial-dependent phases during the course of the acquisition given by $\exp(ik\cdot r)$, with $k = \int_0^{t_2} \gamma_a G_a(t)\, dt$. On comparing these acquisition phases with the $C\Omega_1(r - r^o)$ encoding factor accumulated by spins during their evolution period, it becomes clear that acquisition gradients have the possibility of "unwinding" the spiral of spin-packets that was present at $t_2 = 0$. A constructive interference among spin-packets will then result whenever $k = -C\Omega_1$ (Figure 2, right-hand panel), leading to a nonzero macroscopic magnetization when considering the whole sample volume. This constructive echoing of the spin-packets will be associated with detectable signals, which constitute the "peaks" observed

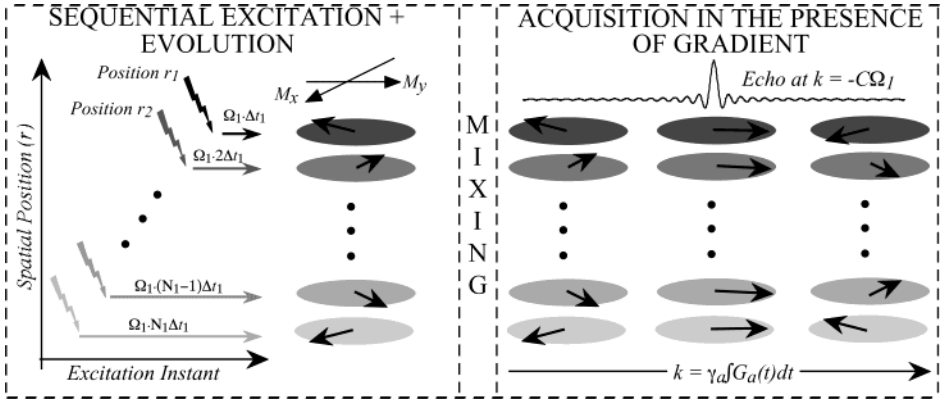

Figure 2. Physical origin of the peaks arising along the indirect dimension of ultrafast 2D NMR experiments. The sequential excitation train that triggers the beginning of t_1 leads to different evolution phases for spins located at inequivalent positions r within the sample. The spiral of spin-packets that is created by this scheme is preserved over the mixing process and can only be unwound during the course of the acquisition by a gradient G_a possessing a spatial dependence identical to that of the excitation gradient. Such unwinding is illustrated on the right-hand side of the figure for just the first of the numerous (N_2) gradient echoes occurring during the acquisition. Illustrated on the top is the sharp echo that is then generated along the k coordinate, whose position reveals the extent of Ω_1 encoding prior to the mixing process and thus the spectral frequency that was active along the indirect dimension.

in this type of experiment along the indirect dimension, and which map along the k-axis the extent of the evolution that occurred prior to the mixing process. Frequencies Ω_2 during the course of the acquisition are then encoded in the usual manner, via the time modulation that these k-peaks exhibit when monitored during the course of a gradient echo train as a function of the time t_2 (Figure 1). A complete 2D NMR data set can thus be recorded within a single scan simply by collecting a unidimensional free-induction decay (FID) under the indicated conditions, rearranging its points into their appropriate (k,t_2) coordinates, and carrying a FT only along the t_2 axis.

A relevant point to notice to proceed with an extension of this ultrafast acquisition scheme to higher dimensionalities is the dissimilar roles that the gradient's strength and the gradient's geometry play in the collection of the data. As is evident from the arguments above, the strengths G_e, G_a will define important range and resolution characteristics of the single-scan 2D NMR spectrum. The actual geometrical distribution of the gradient, in contrast, is mostly responsible for relatively minor line shape characteristics related to the sharpness of the echo formation. Indeed, most of the $r = z$ arguments employed in our previous descriptions[14,15] will remain equally valid if the gradient used to encode and decode the Ω_1 frequencies were assumed to be applied along the $r = x$ or y directions. In either case a spiral of spin-packets would be created by the selective excitation protocol illustrated in Figure 1; even if for a cylindrical profile, the use of radial (x or y) gradients would end up giving different relative weights $A(r)$ to the various spin-packets into which the sample is partitioned. In fact, the only demand that the performance of this kind of experiment places on a gradient's geometry is that it should generate a spiral of spin-packets that is convoluted enough to result in a null magnetization when considered over the whole sample. In principle, there are infinite geometries capable of fulfilling such conditions, including among others those represented by the boundless $\{Y_{l,m}(\theta,\phi)\}$ series of real spherical harmonics of the kind present in modern high-resolution NMR shim systems.[16] Thus, if one assumes a generalized field gradient possessing $Y_{l,m}$ spatial dependence and $G = \partial B_o/\partial(Y_{l,m})$ strength, all arguments leading to eq 2 can be repeated to derive a macroscopic magnetization that at the conclusion of the t_1 evolution period can be summarized as

$$M(N_1\Delta t_1) = \int_x \int_y \int_z A(x,y,z)\cdot e^{iC\Omega_1(Y_{l,m}-Y^o_{l,m})}\,dx\,dy\,dz \qquad (3)$$

This equation represents a winding of spin-packets, arranged this time along the gradient's $Y_{l,m}$ geometry and possessing nonuniform $A(x,y,z)$ weights. Such winding will once again lead to an overall zero magnetization when considering an Ω_1 chemical shift evolution and integration over the whole sample. The same $Y_{l,m}$ gradient used to achieve the spatial encoding in eq 3, however, holds the key for unwinding this spiral of spin-packets and, consequently, for the generation of an observable echo during the course of the acquisition. To achieve this unwinding, spins should be allowed to accumulate a phase $\exp(ik\cdot Y_{l,m})$, with $k = \gamma_a \int G_a(t)\,dt = -C\Omega_1$, during the course of each acquisition dwell time Δt_2. Just as with the z-based examples given in our previous papers, this spatial helix of spin-packets can be wound and unwound numerous times by periodically reversing the $Y_{l,m}$ acquisition gradient, in a process that will encode the spin frequencies as a function of t_2 and thereby enable the collection of 2D NMR spectra within a single scan. The actual shapes of the resulting k-echoes, shapes which will in turn define the kind of peaks observed in ultrafast experiments along the indirect domain, are compared in Figure 3 for a number of cases involving a conventional cylindrical sample and gradients possessing differing spatial dependencies. Also shown is the expected dependence of the echo positions upon changing the site's Ω_1 chemical shift. As can be appreciated from this figure, numerical simulations reveal a behavior that overall is uniform, with minor line shape differences which can be rationalized in terms of the characteristics assumed for the gradients and the sample. These considerations, as well as additional analytical line shape derivations for simple uniaxial gradient cases, are presented below in the Appendix.

Spatial Encoding along Linearly Independent Geometries: Ultrafast 3D NMR

The previous section described the principles by which selective pulses applied in combination with arbitrary gradient geometries can be used to spatially encode indirect-domain t_1

(16) Golay, M. J. E. *Rev. Sci. Instrum.* **1958**, *29*, 313.

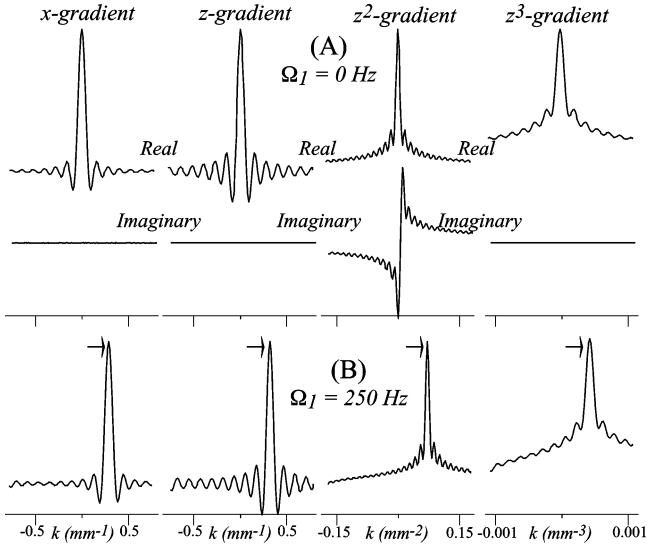

Figure 3. *S*(*k*) line shapes describing the peaks expected along the indirect dimensions of single-scan 2D NMR experiments, when executed using a variety of different gradient geometries. All plots were calculated numerically assuming that spins were in a cylindrical sample, distributed over 300 equally spaced values along the relevant (*x* or *z*) spatial axis. Other parameters, common to all simulations, include 20 N_1 initial excitation slices, a 1.6 cm sample length and diameter, and *k* values spanning the equivalent of a 1.28 kHz spectral width (centered at $k = 0$). (A) Real and imaginary line shape components calculated for $\Omega_1 = 0$. (B) Phased line shapes calculated assuming that a 250 Hz internal chemical shift was active during t_1, with arrows indicating the extent of the echo displacement.

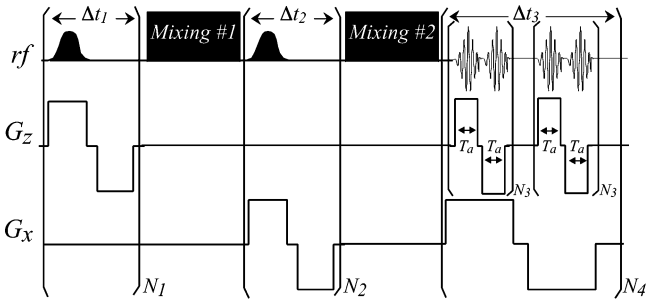

Figure 4. Basic scheme proposed for the single-scan collection of 3D NMR spectra. A train of frequency-shifted pulses is first applied to achieve the spatial encoding of spins throughout different axial positions in the sample (t_1); this is followed by a second rf-driven encoding of the spin evolution during t_2 along a linearly independent radial direction. Data are finally collected while in the presence of oscillating acquisition gradients, which decode the initial Ω_1, Ω_2 frequencies along the (k_z/ν_1,k_x/ν_2) axes while monitoring the spin evolution along a third (t_3) time axis.

evolution frequencies in 2D NMR. An important point to remark is the requirement that this method places on the gradients used to impose the initial spatial encoding and subsequent decoding of these frequencies: only if these geometries are identical will the acquisition gradient succeed in unraveling the winding imposed during the course of the excitation. In contrast, the application of an intermediate gradient that is orthogonal to that employed in the initial excitation will neither add nor detract from the unwinding demands placed on the acquisition gradient. This in turn opens up a route for extending the protocol introduced in the preceding section to include the encoding of an additional indirect dimension, if modified as illustrated in Figure 4. Such a scheme incorporates two separate gradients arranged along linearly independent geometries, which implement two consecutive spatial encodings of the spin evolution. Each one of these encoding processes, assumed here for simplicity to lie along the *x* and *z* directions, proceeds independently and along an outline similar to that described previously for the single-axis 2D NMR experiment. The first of these gradients will thus induce an $\Omega_1 t_1$-dependent winding of the spin-packets along the *z* direction, while for each one of these *z* slices the second gradient will generate an $\Omega_2 t_2$-dependent encoding along the *x* axis. Because of the ensuing "double-winding" of spin-packets, the overall bulk magnetization is again reduced to zero, and an acquisition process implemented on the resulting sample will be associated with a null initial signal. Moreover, in contrast to the 2D encoding case, no single-axis gradient would be capable by itself of regenerating an observable signal from such an initial state. Only the simultaneous application of G_z, G_x acquisition gradients can succeed in aligning the spin-packets, wound as they now are along two orthogonal encoding directions. To find the conditions leading to such an alignment, we implement an echo-planar protocol where both *x* and *z* gradients are rapidly and independently oscillated.[17] The digitized signal can then be regarded as a function of three independent variables: $k_z \propto \int G_z(t)\,dt$, $k_x \propto \int G_x(t)\,dt$, and a time t_3 associated with the final free evolution frequency Ω_3. Figure 5A illustrates how the relevant (k_z,k_x,t_3) space is rastered during the course of this acquisition. Notice that most of the time the digitized signal will be null; yet when the *k*-wavenumbers happen to fulfill the $k_z = -C_z\Omega_1$ and $k_x = -C_x\Omega_2$ conditions, spin-packets throughout the sample will interfere constructively and result in an observable echo. FT of this sharp 2D echo signal along the remaining t_3 dimension provides then a mean for characterizing all (Ω_1,Ω_2,Ω_3) evolution frequencies experienced by the spins throughout the course of the experiment, from data collected within a single scan. Because the mechanisms by which peaks originate in this kind of 3D NMR experiments are identical to those that were earlier described for ultrafast 2D NMR acquisitions,[15] most of the arguments used to derive Nyquist and line shape criteria along the indirect dimension of the latter can be directly extrapolated to the indirect dimensions of the former; consequently their derivation will not be here repeated. For the sake of clarity, however, we have calculated the spins' excitation and acquisition processes throughout model 3D NMR experiment via exact numerical integrations of Bloch equations for spins distributed at different coordinates within the sample. The results which came out from these calculations for sites possessing differing chemical shifts were summarized as Quicktime movies of magnetizations precessing in Bloch spheres; such animations can be downloaded by accessing the Supporting Information web page.

To put these theoretical concepts to the test, a series of basic measurements were carried out. A Bruker Avance 800 MHz NMR spectrometer incorporating a triple-axes inverse gradient probehead was employed as the testing equipment. After the gradients' maximum strengths ($G_z \approx 62$ G/cm, $G_x \approx 37$ G/cm), typical switching times ($\sim 10\ \mu$s), and sample dimensions (1.8 cm length, 0.49 mm diameter) were calibrated, a series of single-scan 3D NMR pulse sequences were written along the guidelines presented in Figure 4. Before describing the results obtained with such sequences, however, we notice that the kind of sampling illustrated in Figure 5A does not provide points distributed over the regular grid needed for fast FT along t_3.

(17) Mansfield, P. *Magn. Reson. Med.* **1984**, *1*, 370.

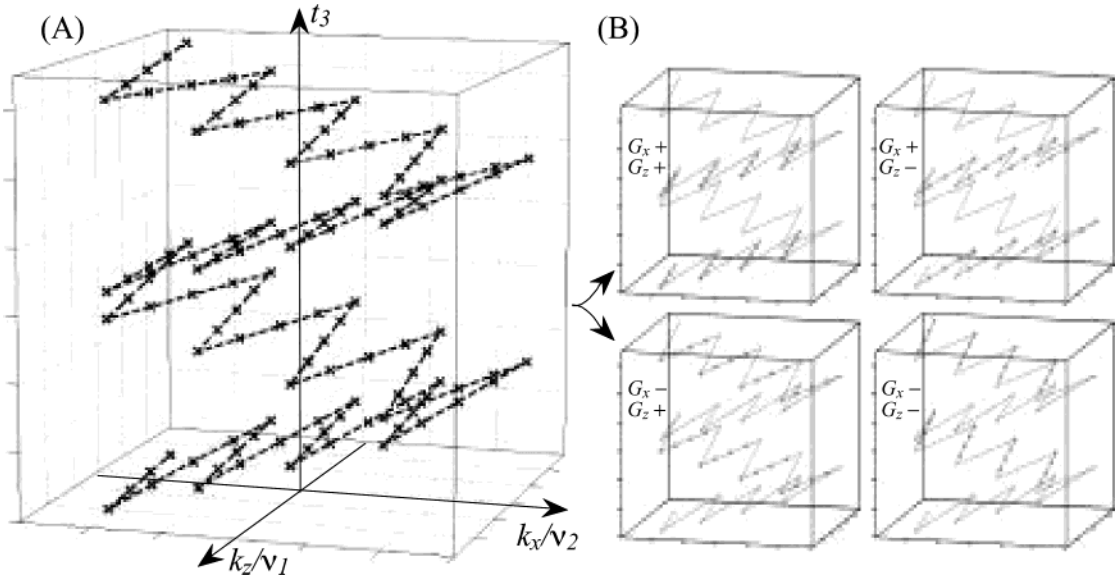

Figure 5. (A) Scanning of the mixed (k_z,k_x,t_3) acquisition space driven by the oscillating-gradient scheme illustrated in Figure 4, assuming for simplicity $N_3 = 4$, $N_4 = 2$. In analogy to the procedure described to process single-scan 2D NMR spectra,[14,15] fast FT of points acquired in such fashion requires a preliminary discrimination of the points according to the $\pm G_x$, $\pm G_z$ values used in their acquisition. This leads to the four independent tridimensional data sets shown in (B). After a FT of these sets along the t_3 axis was implemented, four symmetry-related spectra are obtained; all of the resulting data sets can be co-added for the sake of improving the overall S/N (a procedure not implemented in this study). All of these data postprocessing procedures were carried out in this study on a 2.4 GHz Pentium IV computer, using custom-written Matlab 6.5 (The MathWorks Inc.) software routines.

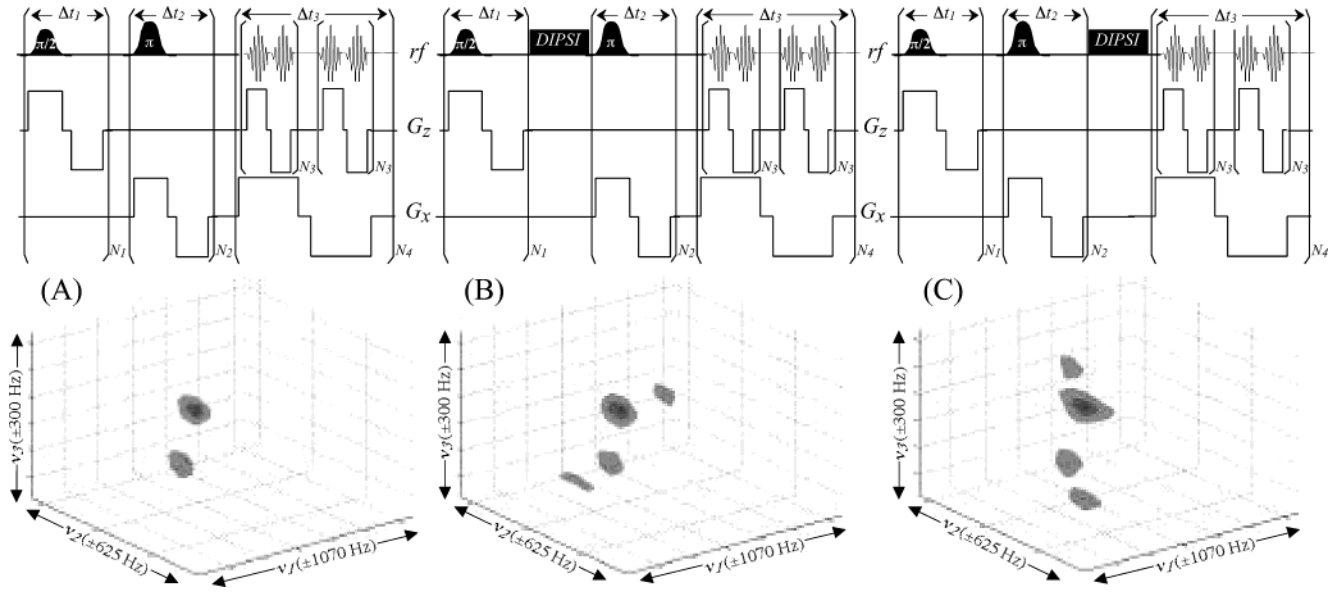

Figure 6. Single-scan 3D NMR spectra acquired on an ~20% w/w *n*-hexane/$CDCl_3$ sample, using the pulse sequences schematized on top of each set. Notice that, due to the absence of a well-defined triggering event, the indirect t_2 evolution was encoded in all cases using a constant-time scheme incorporating an incremented refocusing π pulse. As for all experiments presented in this study, these experimental data were acquired on a Bruker NMR spectrometer using a triple-axis QXI probehead. Other acquisition parameters included 25 64-μs-long $\pi/2$ pulses applied at 8 kHz offset increments while in the presence of a 110 kHz/cm *z* gradient, 11 128-μs-long π pulses applied at 4 kHz increments while in the presence of a 80 kHz/cm *x* gradient, and an acquisition period where 6 N_3 *z*-gradient echoes were nested within 16 N_4 *x*-gradient echoes. Data were scanned with $T_a = 64$ μs (plus 5 μs gradient switching times) and 1.5 μs physical dwell times; maximum gradient strengths during these acquisitions were set to 103 and 16 kHz/cm along the *z* and *x* directions, respectively. Such conditions yielded $46 \times 6 \times 16$ points in the mixed (ν_1/k_z, ν_2/k_x, t_3) domain, together with the indicated spectral width values. For their spectral presentation, data were then separated as illustrated in Figure 5, back-FT'd along ν_1 and ν_2, linear-predicted in the resulting time-domain to $128 \times 16 \times 32$ points, forward FT'd into the 3D frequency domain, and presented in magnitude mode. For the experiments shown in panels (B,C), DIPSI mixing periods of 40 ms were inserted at the indicated positions.[18,19] Total acquisition times were ca. 30 ms for the 3D NMR experiment shown in (A), and 70 ms for the spectra in (B,C).

To cope with this complication, data were subjected to a rearrangement/separation procedure analogous to that previously described for the 2D NMR case[14] prior to this transformation. This demand of the ultrafast 3D NMR protocol to separate data into four independent subsets (Figure 5B), coupled to the relatively weak gradient strengths that were available in the spectroscopic probehead used to test these experiments, implied that relatively long periods of time had to be spent to sample appropriate excursions along the k_z and k_x axes. This in turn imposed a penalty on our 3D acquisitions in the form of long dwell times along t_3. Compromises were made to alleviate this penalty, particularly in terms of the number of points that were sampled along two of the spectral dimensions, and of the spectral widths that could be accommodated.

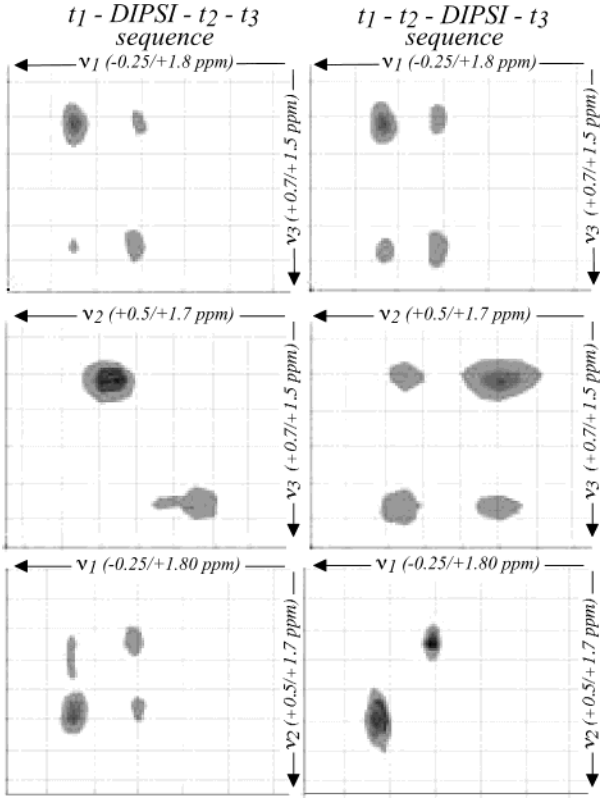

Figure 7. Contours extracted along the indicated dimensions, by projecting (skyline) the single-scan 3D NMR data illustrated in Figure 6B, 6C against the remaining spectral axis. Gray scale contours begin at 20% of the maximum signal intensity. Also indicated are the chemical shift ranges (in ppm from TMS) covered by each spectral axis.

Practical limitations notwithstanding, Figures 6 and 7 illustrate proof-of-principle results on the feasibility of implementing single-scan 3D NMR, utilizing ^{1}H experiments on an *n*-hexane/$CDCl_3$ sample as a model. Because of the limited spectral resolution available in these tests, only two out of the three inequivalent sites in this compound could actually be resolved: a peak for the methyl protons (0.89 ppm) and another one for all of the methylenes (1.28 ppm). Figure 6A illustrates with an isosurface cube representation the results observed upon testing a single-scan 3D NMR sequence possessing no actual mixing processes. As no pulses are involved in the t_1/t_2 transition, a constant-time version of the experiment was implemented to impart the second spatial encoding. All peaks appear then aligned along the main diagonal, reflecting the identical Ω_1, Ω_2, and Ω_3 frequencies that were active during the course of the evolution. In contrast, Figure 6B and 6C illustrates results observed upon introducing into this experiment an isotropic mixing sequence between the various evolution periods.[18] A number of cross-peaks appear in these plots between the methyl and methylene peaks, as expected on implementing 3D TOCSY NMR on such a compound. Figure 7A and 7B expands on these results by illustrating various 2D views of results obtained upon inserting a single isotropic mixing period within the different periods of the experiment. Cross-peaks between methyl and methylene peaks appear in these cases, yet only along the expected pairs of spectral axes. In unison, all of these results corroborate the proper operation of the single-scan 3D NMR scheme.

(18) Braunschweiler, L.; Ernst, R. R. *J. Magn. Reson.* **1983**, *53*, 521.

Experiments such as those illustrated in Figures 6 and 7, involving solely homonuclear correlations, do not reflect the majority of 3D NMR sequences. In most instances, the power of 3D NMR stems from exploiting the superior resolution that these experiments may achieve when they incorporate a heteronuclear evolution period.[6] The spatial encoding principles detailed in the preceding section can also be employed for implementing this kind of heteronuclear correlation. Such experiments would then rely on the coherent nature of heteronuclear $S \rightarrow I$ transfers, which will preserve the spatial encoding imparted by a train of rf pulses even while the nature of the nuclei that carry such encoding changes, in order to parallelize the manner by which the heteronuclear evolution is encoded. Figure 8 (top) illustrates a pulse sequence based on such a premise, designed to collect a 3D NMR spectrum within a single scan and containing an HSQC evolution during the course of its second evolution period. Also illustrated in the figure are results obtained with such a sequence on a glycerol sample. The pulse sequence used in this experiment entailed (i) an initial ^{1}H t_1 evolution that is spatially encoded along the *x* direction; (ii) an INEPT block[20] where such encoding is transferred from a given ^{1}H to its directly bonded ^{13}C; (iii) a selective $(\pi/2)_C$ pulse applied under the action of a *z* gradient, whereby the $H_zC_z \rightarrow H_zC_x$ conversion is triggered and the ^{13}C t_2 evolution becomes spatially encoded; (iv) an INEPT back-transfer to the bonded ^{1}H; and (v) a final signal acquisition period implemented while scanning the k_x, k_z, and t_3 axes. Throughout the whole pulse sequence, heteronuclear decoupling was implemented with the aid of on-resonance π-pulses applied in synchrony with the zero-crossings of the various gradients. On calculating two-dimensional projections out of this 3D data only diagonal peaks are observed when monitoring the data along the ν_1/ν_3 ^{1}H evolution dimensions, as transfers to the carbon spins were only made from and to their directly coupled neighbors. Three peaks are also observed upon calculating the 2D heteronuclear projections along the ν_2/ν_3 or ν_2/ν_1 axes: two corresponding to inequivalent protons bonded to glycerol's C1/C3 carbons and another one arising from the central CHOH moiety.

As a further example of this single-scan 3D NMR methodology, Figure 9 illustrates the results obtained upon implementing a full TOCSY-HSQC experiment on the glycerol sample. Such an experiment proceeds just as that described in Figure 8, except for the inclusion of an isotropic mixing sequence between the indirect t_1 and t_2 evolution periods. As all protons in the glycerol molecule are mutually coupled, such a block results in all ^{1}H resonances ending up correlated among themselves. Instead of the three resonances that arise in the pure HSQC spectrum, nine peaks result from imparting this additional correlation; this feature can again be clearly appreciated from the various views presented in Figure 9.

Single-Scan NMR with an Arbitrary Number of Spectral Dimensions

Having discussed how the principles of single-scan 2D NMR can be extended to a third dimension and illustrated the execution of these experiments with a number of simple examples, this final section considers how these principles can be generalized to an arbitrary number of dimensions. Such a

(19) Shaka, A. J.; Lee, C. J.; Pines, A. *J. Magn. Reson.* **1988**, *77*, 274.
(20) Morris, G. A.; Freeman, R. *J. Am. Chem. Soc.* **1979**, *101*, 760.

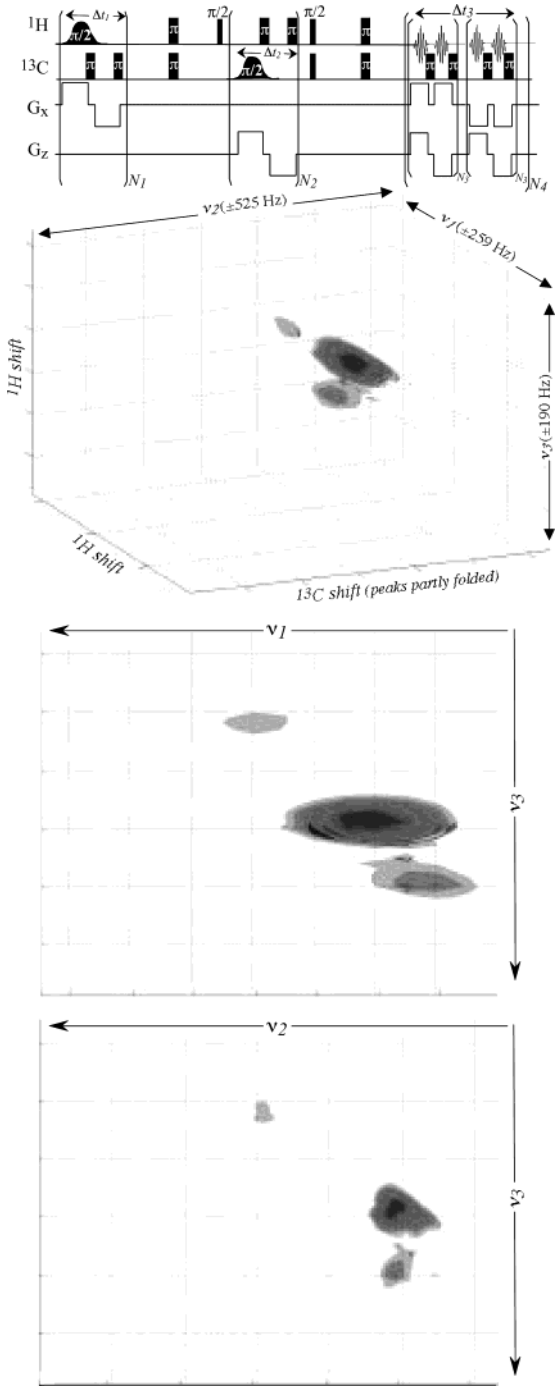

Figure 8. Single-scan 3D NMR spectrum acquired on a 98% ^{13}C-enriched glycerol/D_2O sample (Spectra Gases), using the HSQC-based pulse sequence indicated on top. In addition to an isosurface representation of the full spectrum (box), 2D contours resulting from projecting the 3D NMR data against the remaining spectral axis are also shown (center and bottom). Excitation parameters included $N_1 = 11$, $N_2 = 17$, all selective pulses 256-μs-long Gaussians applied at 4 kHz offset increments, a 160 kHz/cm z gradient, and a 100 kHz/cm x gradient. Initial and final heteronuclear transfer periods were set at 1.75 and 1.40 ms, respectively. Acquisition parameters included $N_3 = 6$, $N_4 = 24$, $T_a = 60$ μs (plus 50 μs for the gradient switching and the ^{13}C π pulse), 1.5 μs physical dwell times, maximum x and z gradient strengths of 63 and 9 kHz/cm, respectively. Such conditions yielded 88 × 6 × 24 points in the mixed (ν_2/k_z, ν_1/k_x, t_3) domain, which were processed as described in Figure 6 into a 128 × 16 × 64-point magnitude spectrum. For the indicated acquisition conditions, it was not possible to cover the 2 kHz range required to fit glycerol's complete ^{13}C frequency extent at 18.8 T, whose peaks were consequently folded into their observed positions by the "ghosting" mechanism described in ref 15. The total time required to carry out this experiment was ca. 81 ms.

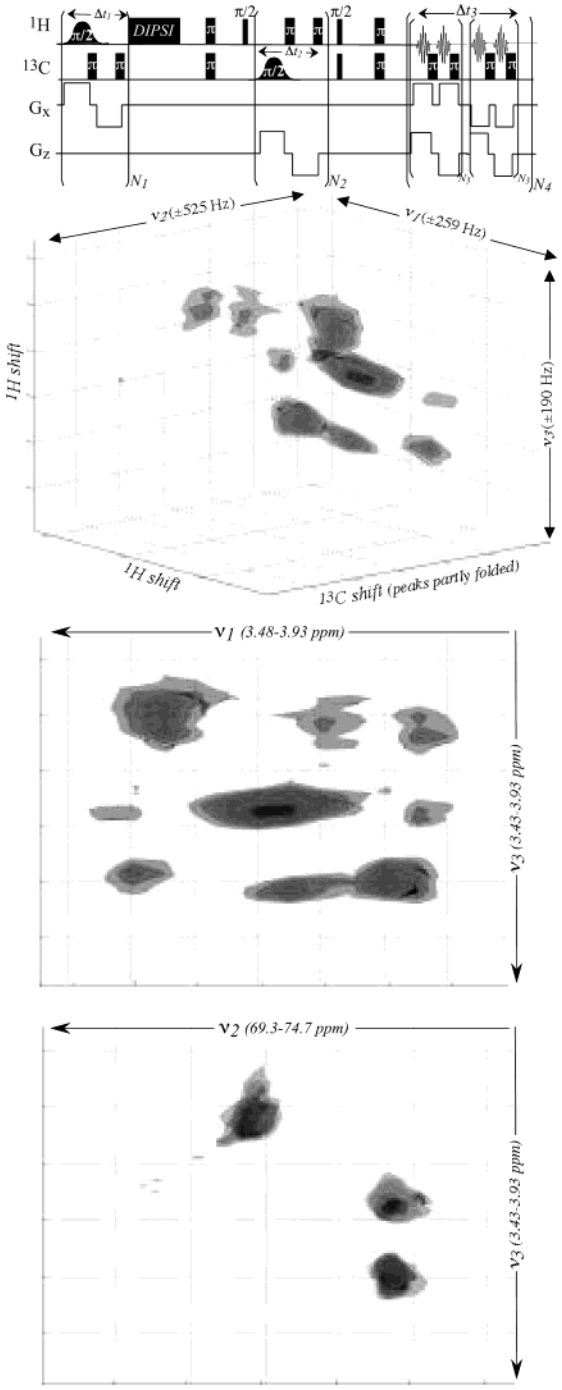

Figure 9. Single-scan 3D TOCSY-HSQC NMR spectrum acquired on a glycerol/D_2O sample, using the pulse sequence indicated on top. All pulse and timing parameters were similar to those summarized in Figure 8, except for the addition of a 60 ms long DIPSI mixing sequence between t_1 and t_2. Presented in the lower panels are skyline projections extracted from the 3D NMR data along the indicated dimensions; also indicated are the chemical shift ranges (in ppm from TMS) covered by each spectral axis. Total experimental time: 141 ms.

generalization is made possible by the countless gradient geometries that can in principle be utilized for encoding the spin evolution, represented for instance by the spherical harmonic set $\{Y_{l,m}\}$ discussed earlier. When applied in combination with a train of frequency selective rf pulses, any of these eigenfunctions can be employed to wind an independent spiral of spin-packets, of the type summarized by the Fourier relation in eq 3. The task of unraveling the spin evolution frequencies

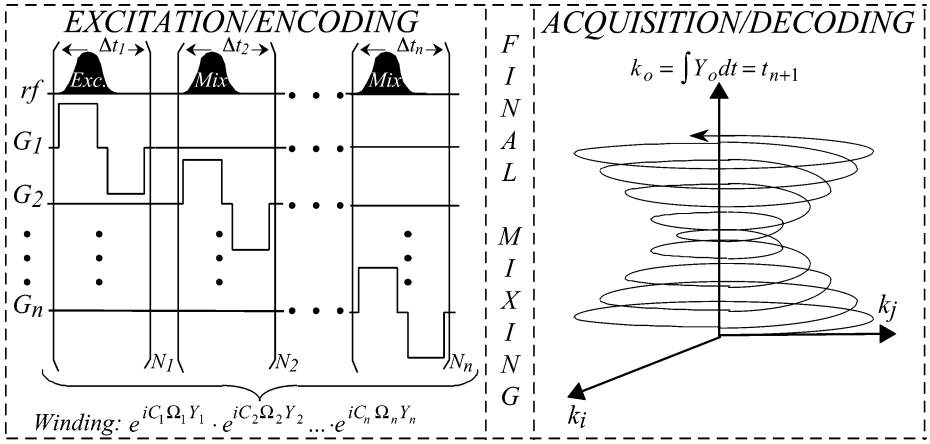

Figure 10. Generic scheme enabling the extension of the single-scan data acquisition strategy put forward throughout Figures 4−9, to what in principle could amount to an arbitrary number of NMR dimensions. The $\{G_i\}_{1\le i\le n}$ represent a set of field gradients possessing linearly independent geometries Y_i; such gradients can spatially encode the frequencies active along the various $\{t_i\}_{1\le i\le n}$ indirect-dimension times involved in the experiment, if applied in combination with frequency selective pulses that trigger their respective evolution periods (or using a constant-time approach like the one indicated in Figure 6A). Following a final, nonselective mixing process, the spatial encoding imparted along all n indirect dimensions needs to be decoded by oscillating all gradients simultaneously while the signal is monitored as a function of the direct t_{n+1} acquisition time (for clarity, only two of the k-axes being rastered are illustrated in the scheme).

which acted along various indirect dimensions becomes then equivalent to scanning simultaneously the multiple $k_{l,m}$ axes associated with these various gradients; such a procedure can in principle always be carried out within a single continuous acquisition, provided that flexible enough gradients are available. Figure 10 summarizes the kind of scheme that would then be involved in these arbitrary n-dimensional experiments. Needless to say, numerous practical complications and limitations can be expected to accompany this kind of acquisition scheme when implemented under realistic conditions: very fast data digitization requirements along multiple independent axes will be associated with losses in S/N, gradient strengths will limit the resolution and spectral ranges that can be characterized along the different domains, switching delays will increase even further the relatively long dwells already characterizing the 3D NMR experiments, etc. Yet it is interesting to note that, at least from a conceptual standpoint, arbitrarily high-dimensional NMR experiments could be acquired in this fashion within a fraction of a second. Figure 11 illustrates 4D NMR results collected on the basis of such principles, with the triple-axis spatial encoding that they required implemented with the aid of x, y, z spectroscopy gradients applied in combination with a constant-time protocol. An ^{15}N-labeled urea sample was used for this basic test, yielding a ^{1}H NMR spectrum consisting of a doublet split by a $J^{15}_{N-^1H} \approx 90$ Hz coupling. A sequence devoid of an actual mixing sequence showed these two proton peaks arranged, as expected, along the main diagonal of the 4D NMR spectrum (Figure 11A). Yet the position and appearance of the resulting doublet along the various spectral axes could be manipulated by introducing periods of ^{15}N rf irradiation between the various t_i/t_{i+1} evolution times (Figure 11B−E), lending experimental backing to the conceptual principles underlying this approach.

Conclusions

It is clear that valuable opportunities would open up if the acquisition times required to collect multidimensional NMR spectra could be reduced. A flavor for the benefits to be reaped from such an accomplishment can be gained from parallel developments in zeugmatographic imaging, where ultrafast 2D NMR acquisitions schemes have enabled a true revolution of the field.[21,22] For a long time, similar efforts have also been underway to accelerate 2D NMR experiments within a purely spectroscopic setting,[23−25] although with mixed practical success. Still, and within the uncertain limits with which such matters can be gauged, a series of recent developments suggest that the future might be brightening up for the accelerated recording of n-dimensional NMR spectra.[14,15,26,27] Among these developments is our proposal of combining the application of longitudinal magnetic field gradient echoes with selective rf excitation sequences, which enable the acquisition of 2D NMR experiments to be completed within a single scan. Such acquisitions can then be carried out while retaining all of the qualities that in terms of resolution and generality are provided by well-proven 2D FT NMR methods. The purpose of the present account was to show how such principles, together with their potential advantages, can be extended to NMR experiments possessing what could in principle amount to arbitrary numbers of spectral dimensions. As for the two-dimensional case, this objective is again achieved by combining selective rf manipulations with spatially dependent magnetic field gradients. Yet when compared to our previous ultrafast 2D NMR contributions, these higher-dimensional schemes exploit another aspect of spatially encoded acquisitions: the role played by the actual geometry of the gradient employed for achieving the spatial encoding during the course of the experiment. The extension of the 2D scheme to higher dimensions is then based on the realization that (i) the spatial encoding of spin evolutions can be implemented using gradients with different geometries; (ii) infinite such geometries can in principle be designed; and (iii) if properly designed gradients are employed to achieve a series of such encodings, the effect imparted by any one gradient can be made

(21) Stehling, M. K.; Turner, R.; Mansfield, P. *Science* **1991**, *254*, 43.
(22) *Echo Planar Imaging: Principles, Technique, Application*; Schmitt, F., Stehling, M. K., Turner, R., Eds.; Springer-Verlag: Berlin, 1998.
(23) Bax, A.; Mehlkoff, A. F.; Smidt, J. *J. Magn. Reson.* **1980**, *40*, 213.
(24) Frydman, L.; Peng, J. *Chem. Phys. Lett.* **1994**, *220*, 371.
(25) Blumler, P.; Jansen, J.; Blumich, B. *Solid State Nucl. Magn. Reson.* **1994**, *3*, 237.
(26) Kim, S.; Szyperski, T. *J. Am. Chem. Soc.* **2003**, *125*, 1385.
(27) Kupce, E.; Freeman, R. *J. Magn. Reson.* **2003**, *163*, 56.

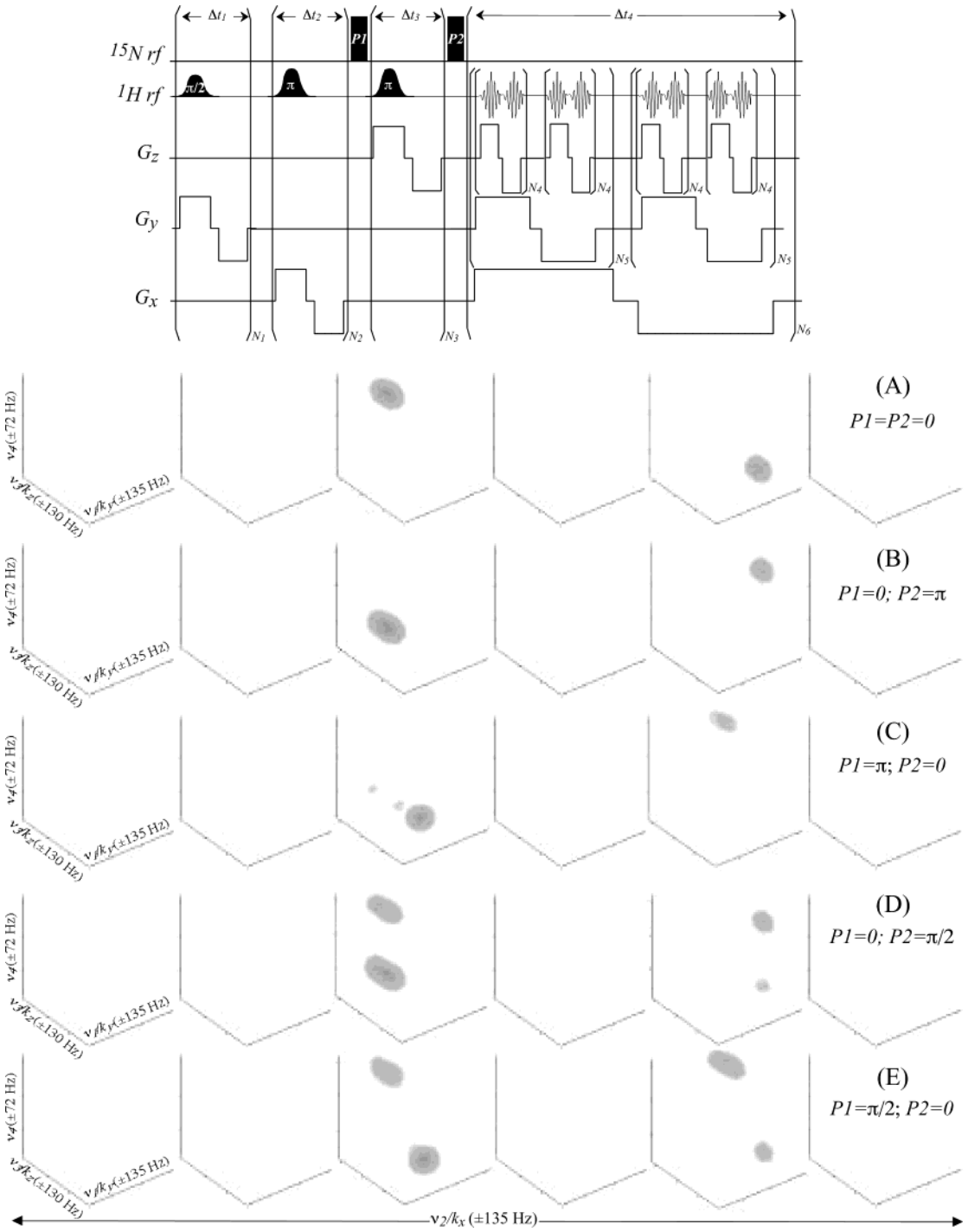

Figure 11. Array of single-scan 4D ^{1}H NMR spectra acquired on a sample of $(^{15}NH_2)_2CO$ (~50 mg, Cambridge Isotopes) dissolved in d_6-DMSO, using the test pulse sequence schematized on top. All spectral dimensions correspond here to ^{1}H evolutions, with mixing periods differing in their treatment of the ^{15}N spins. (A) Spectrum devoid of actual mixing sequence, showing the two peaks of the ^{1}H−^{15}N doublet arranged along the main diagonal of the 4D spectral space (each of the displayed cubes corresponds to a single point along k_x). (B) The same as in (A) but with the application of a $(\pi)_N$ pulse reversing the identity of the ^{15}N spin states prior to t_4. (C) The same as in (A) but with the $(\pi)_N$ pulse applied between t_2 and t_3. (D,E) The same as in (C) but with the ^{15}N pulses now set to $\pi/2$, thereby splitting the identity of the proton resonances for the remainder of the experiment. Excitation parameters included $N_1 = N_2 = 19$, $N_3 = 25$; all selective pulses had rectangular shapes and were 500-μs-long with 2.2 kHz offset increments and $\gamma_e G_e = 82$ kHz/cm for the radial axes, and 250-μs-long with 4 kHz offset increments and $\gamma_e G_e = 54$ kHz/cm for the longitudinal axis. The on-resonance $(\pi)_N$ pulses were 82 μs long. Acquisition parameters included $N_4 = N_5 = N_6 = 6$, $T_a = 18$ μs (plus 6 μs for gradient switching), 2.0 μs physical dwell times, and maximum x, y, and z gradient strengths of 11.2, 48, and 162 kHz/cm, respectively. Under such conditions and due to the fact that data had to be separated along eight $\pm G_a$ sets prior to FT processing (two per indirect domain, cf. Figure 5), only ~140 Hz resulted as spectral width along the direct domain. 6 × 6 × 12 × 6 points in the mixed (ν_1/k_y, ν_2/k_x, ν_3/k_z, t_4) domain were thus obtained, processed as described in Figure 6 into the displayed 16 × 6 × 32 × 16 point magnitude spectrum, and displayed as isosurfaces with a 35% minimum threshold. The total experimental time of each of these single-scan 4D NMR acquisitions was 94 ms.

independent from those imparted by the remainder of the series. On considering that the effects imparted by several encoding gradients can be simultaneously decoded via the application of echo-planar spectroscopic protocols,[17] it follows that the number

of dimensions that can be simultaneously accessed in this fashion within a single continuous acquisition becomes a priori limitless. Experimental examples of this generalization were given on the basis of the $x-y-z$ gradients normally available in spectroscopic (or microimaging) settings; yet the potential use of less conventional gradients for achieving such goals is also worth considering.

As mentioned earlier, numerous practical challenges are scattered along the road that single-scan NMR would have to transverse before it can be routinely employed in higher-dimensional acquisitions. Spectral resolution, range, and S/N are among the main targets to be improved for bringing the full potential of these acquisition schemes to bear on routine chemical, biochemical, or medical contexts. Some of these improvements could be achieved with the introduction of suitable hardware, including stronger and faster switching gradients than those currently available in spectroscopic equipment. For instance, increasing the gradient strength available along a particular spatial direction could enable increasing the number of excitation cycles along that direction and consequently a lengthening of its associated evolution time, bringing about a concomitant narrowing of the peaks resulting along that dimension. Similar arguments could be invoked in connection to enhancing gradients and thereby achieving an increase in the accessible spectral range. Additional improvements in sensitivity and in other spectral characteristics should result from data processing schemes that, unlike the scheme sketched in Figure 5, do not employ a small fraction of the available data (25% in the case of 3D NMR; only 12.5% for the 4D NMR) for retrieving the final spectrum. Progress can also be expected from alternative modes of collecting single-scan multidimensional NMR data, which although based on the principles noted in this manuscript might differ in the modalities used for the spin excitation and for the spatial encoding. Still, it is interesting to speculate even at this time on what the detection capabilities of such a mode of analysis would be. To do so, we focus on a typical ^{1}H-detected nD NMR experiment involving an amplitude modulation of the signals along all indirect domains and use as starting point for the limit of detection analysis the S/N quoted by a main NMR spectrometers manufacturer: 1750:1 for a single-pulse 1D ^{1}H NMR experiment on a 0.1% ethylbenzene/$CDCl_3$ solution at 18.8 T. The main S/N penalties that will affect this figure upon implementing a single-scan nD NMR experiment will stem from the gradient-driven coherence filtering associated with the various mixing processes, and from the need to open up the spectrometer's frequency filter width wide enough to accommodate during the data acquisition a sampling of points along all of the ν_i/t axes simultaneously. For the case of an nD single-scan NMR experiment, the first of these factors will scale signals by ca. $(0.5)^{n-1}$ while the latter will magnify noises by ca. 5^{n-1}, transforming the S/N ratio quoted above into ~19:1 for a 3D NMR experiment on a 10 mM sample. This is a sufficient limit of detection for several interesting applications; yet it is only marginal when considering biomolecular protein NMR studies where aqueous ^{1}H measurements tend to have worse S/N than their organic counterparts, and where 10 mM usually lies beyond the aggregation limit for several medium-sized systems. On the other hand, the same analysis suggests that within a minute-long acquisition period involving the collection of 30−60 scans, quality 3D protein NMR spectra could become available from solutions in the 1−10 mM concentration range. We believe that overall these are promising results which could open novel and untapped applications for high-throughput high-dimensional NMR, in areas that until recently might have seemed beyond the realm of this methodology.

Acknowledgment. We are grateful to Dr. Adonis Lupulescu (Chemical Physics Department, Weizmann Institute) for insightful discussions, to Mr. Ilija Uzelac (K. Kupcinet 2002 Summer School, Weizmann Institute) for assistance in writing the spin propagation programs and computing the animations illustrated in the Supporting Information, and to Dr. Tali Scherf (Chemical Services, Weizmann Institute) for assistance in setting up the experiments here described. This work was supported by the Philip M. Klutznick Fund for Research, by the Minerva Foundation (Munich, FRG), as well as by a grant from the Henry Gutwirth Fund for the Promotion of Research.

Appendix: Analytical Derivations of *k*-Space Line Shapes for Various Gradient Geometries

As follows from the arguments presented in the paper, the line shapes observed along the indirect domains of ultrafast 2D NMR experiments are dictated by the signals observed for a fixed Δt_2 dwell value and as a function of $k = \int_0^{t \le \Delta t_2} \gamma_a G_a(t')\, dt'$. Within a first approximation that neglects the inner mechanism of the rf excitation (such as nonlinear effects depending on the pulses' shape), these $S(k)$ signals can be described as a sum throughout the sample volume, of contributions arising from the various spin-packets onto which the sample has been partitioned by the initial train of selective excitation pulses. As denoted in eq 3, these spin-packets will have evolved discrete t_1 phases that are spatially dependent and possess magnitudes $A(x,y,z)$ that are also voxel-dependent. Following the mixing process, these different spin-packets will also be affected by distinct spatially dependent k evolutions. All of these considerations can be taken into account simultaneously by relatively simple computer simulation programs that partition the sample into a large number of voxels and, as was done within the context of Figure 3, are used to derive numerically the peak shapes expected for a particular spatial dependency of the gradient. Yet as demonstrated in a preceding publication for the particular case of a linear z gradient, one can also attempt to derive analytical expressions for the $S(k)$ line shape;[15] the purpose of the present Appendix is to provide a framework for the analytical derivation of line shapes when dealing with the more complex gradient geometries required for carrying out single-scan higher-dimensional NMR experiments. Toward this end, we begin by assuming that both the excitation and the acquisition gradients G_e, G_a possess arbitrary but identical $Y_{l,m}(x,y,z)$ spatial dependencies. The signal that is then collected as a function of k can be written as

$$S(k) = \int_{-L/2}^{L/2} dz \iint_{x^2+y^2 \le R^2} dx\, dy A(x,y,z) \cdot e^{i\Omega_1 t_1(Y_{l,m}(x,y,z))} e^{ikY_{l,m}(x,y,z)} \tag{A1}$$

where for the sake of simplicity we have assumed a cylindrical sample geometry. The t_1 time appearing in this equation is actually a linear and discrete function of $Y_{l,m}$, which can be written as $t_1(Y_{l,m}(x,y,z)) = [Y_{l,m}(x,y,z)/\Delta(Y_{l,m})]\Delta t_1$, $\Delta(Y_{l,m})$ being a generalized "slice" increment given by $\Delta O/(\gamma_e G_e)$. When

placing t_1 into eq A1, it is clear that $S(k)$ will become a maximum whenever $\Omega_1 \cdot \Delta t_1/\Delta(Y_{l,m}) + k$ is a multiple of 2π, a condition defining the positioning of the $S(k)$ peaks and of their associated "ghosts". Equation A1, however, also shows evidence that the actual shape of this echo along the k-axis will be given by an FT of $A(x,y,z)$ against $Y_{l,m}$, an integral which in general will not be trivial to calculate analytically for arbitrary spatial dependencies of the gradient. Still, we found it feasible to derive closed-form results when the gradients can be expressed as either $Y(x)$, $Y(y)$, or $Y(z)$, simple uniaxial geometries which we consider from here on. The functions to be integrated in eq A1 are then restricted to a single variable, while integration along the remaining two axes serves only as an additional weighting factor (which is a constant for z-axis gradients, and semicircular for either x- or y-gradients). To proceed with this integral's calculation, we implement in eq A1 the variable change $\{x,y,z\} \rightarrow \{Y(u),\upsilon,w\}$, where u is the dimension involved in defining the gradient's geometry and υ, w are the remaining "nonactive" spatial axes. Carrying out an integration over these remaining axes provides a weighting function $W(u)$ and a signal expression

$$S(k) = \int_{u_{\min}}^{u_{\max}} du W(u) e^{i\Omega_1 t_1(Y(u))} e^{ikY(u)} \qquad \text{(A2)}$$

To calculate this expression, it is also necessary to account for the different "thicknesses" of the various slices excited for a constant offset increment ΔO as a function of the gradient's $G_a Y_{l,m}$ frequency. This is taken care of by changing the integration variable in eq A2 from u to $\alpha = Y_{l,m}(u)$, resulting in

$$S(k) = \int_{\alpha_{\min}}^{\alpha_{\max}} d\alpha \left[\frac{d\alpha}{du}\right]^{-1} W(Y^{-1}(\alpha)) e^{i\Omega_1 t_1(\alpha)} e^{ik\alpha} \qquad \text{(A3)}$$

We employ this expression to calculate line shape expressions for gradients involving a generic z^n, as well as linear x/y spatial dependencies. The former treatment needs in turn to be subdivided into two subcases depending on whether n is even or odd; we treat in most detail the even n situation. In this case, any given excitation pulse will affect both $\pm z$ coordinates; this symmetry reduces eq A3 to

$$S(k) = \frac{2M_o}{nL} \int_0^{\left(\frac{L}{2}\right)^n} d\alpha \cdot \alpha^{(1/n)-1} e^{i\Omega_1 t_1(\alpha)} e^{ik\alpha} \qquad \text{(A4)}$$

The fact that t_1 is actually a discrete variable can now be introduced, and the integral can be cast as a sum over the N slices of thickness $\Delta\alpha = \Delta O/(\gamma_e G_e)$ onto which the sample was partitioned by the rf pulses; that is,

$$S(k) = \frac{2M_o}{nL} \sum_{m=0}^{N-1} e^{im\Omega_1 \Delta t_1} \int_{m\Delta\alpha}^{(m+1)\Delta\alpha} d\alpha \cdot \alpha^{(1/n)-1} \cdot e^{ik\alpha} \qquad \text{(A5)}$$

A closed-form expression can then be reached if eq A5 is rewritten as a difference between two integrals within the $x \in [0,1]$ range:

$$\begin{aligned} S(k) &= \frac{2M_o}{nL} \sum_{m=0}^{N-1} e^{im\Omega_1 \Delta t_1} \{[(m+1)\Delta\alpha]^{(1/n)} \times \\ &\quad \int_0^1 dx \cdot x^{(1/n)-1} e^{ik(m+1)\Delta\alpha x} - (m\Delta\alpha)^{(1/n)} \times \\ &\quad \int_0^1 dx \cdot x^{(1/n)-1} e^{ikm\Delta\alpha x}\} \qquad \text{(A6)} \\ &= \frac{2M_o}{nL} \sum_{m=0}^{N-1} e^{im\Omega_1 \Delta t_1} \times \\ &\quad \left\{[(m+1)\Delta\alpha]^{(1/n)} {}_1F_1\left(\frac{1}{n}; \frac{1}{n}+1; ik(m+1)\Delta\alpha\right) - \right. \\ &\quad \left. (m\Delta\alpha)^{(1/n)} {}_1F_1\left(\frac{1}{n}; \frac{1}{n}+1; ikm\Delta\alpha\right)\right\} \end{aligned}$$

One thus obtains a general analytical line shape expression as a function of the generalized ${}_1F_1(a;b;c)$ hypergeometric function.[28] A similar treatment for n odd leads to

$$\begin{aligned} S(k) = \frac{e^{i(N/2)\Omega_1 \Delta t_1} M_o}{nL} \sum_{m=0}^{(N/2)-1} \\ \left\{ e^{-i(m+1)\Omega_1 \Delta t_1} \left\{ \begin{array}{c} [(m+1)\Delta\alpha]^{(1/n)} {}_1F_1\left(\frac{1}{n}; \frac{1}{n}+1; -ik(m+1)\Delta\alpha\right) \\ -(m\Delta\alpha)^{(1/n)} {}_1F_1\left(\frac{1}{n}; \frac{1}{n}+1; -ikm\Delta\alpha\right) \end{array} \right\} \right. \\ \left. + e^{im\Omega_1 \Delta t_1} \left\{ \begin{array}{c} [(m+1)\Delta\alpha]^{(1/n)} {}_1F_1\left(\frac{1}{n}; \frac{1}{n}+1; ik(m+1)\Delta\alpha\right) \\ -(m\Delta\alpha)^{(1/n)} {}_1F_1\left(\frac{1}{n}; \frac{1}{n}+1; ikm\Delta\alpha\right) \end{array} \right\} \right\} \qquad \text{(A7)} \end{aligned}$$

When applying x or y gradients, the shape of the sample ends up appearing as part of the integrand in eq A3:

$$S(k) = \frac{M_o}{R} \int_o^{2R} dx \sqrt{R^2 - (x-R)^2}\, e^{i\Omega_1 t_1(x)} e^{ik(x-R)} \qquad \text{(A8)}$$

The square root form of the weighting function prevented us from deriving an exact form for the integral. Instead, an analytical form was computed using an approximation whereby the intensity within each of the excited slices was assumed to vary linearly over the extent of each Δx slice. Such "binning" of the sample shape then leads to

$$\begin{aligned} S(k) = M_o \sqrt{\frac{4}{N}}\, e^{ik(N/2)-1)\Delta x/2} \sum_{m=0}^{N-1} e^{i(\Omega_1 \Delta t_1 + k\Delta x)m} \times \\ \left\{ a_m \Delta x\, \mathrm{sinc}\left(\frac{k\Delta x}{2\pi}\right) - \frac{a_{m+1} - a_m}{ik}\left[\mathrm{sinc}\left(\frac{k\Delta x}{2\pi}\right) - e^{ik_x \Delta x/2}\right]\right\} \qquad \text{(A9)} \end{aligned}$$

where $a_m = \sqrt{m - ((m^2/N))}$.

To examine the accuracy (and hence the usefulness) of the various expressions derived in this Appendix, their predictions were computed for various gradient profiles. A frequency

(28) *Tables of Integral Transforms*; Bateman, H., Ed; McGraw-Hill: New York, 1954; Vol. 1, p 187.

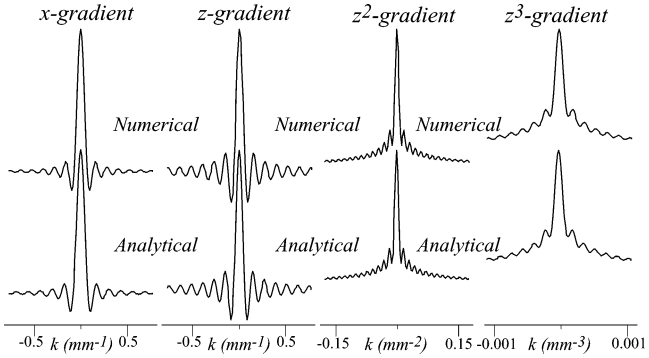

Figure 12. Comparison between $S(k)$ line shapes calculated numerically as described in Figure 3 for various gradient geometries, and predictions calculated from the analytical expressions in this Appendix. All line shapes were calculated using settings identical to those presented in Figure 3.

$\Omega_1 = 0$ kHz was assumed; other relevant parameters included sample length and diameters $L = 2R = 16$ mm, a total number of slices $N = 20$, and 128 digitized points corresponding to a first cycle of positive gradient acquisition only. Figure 12 compares the plots arising from the analytical derivations in eqs A6, A7, and A9, and "brute force" numerical results. As can be seen, the agreement between both data sets is excellent.

It is worth concluding by remarking that a number of differences were observed when comparing line shapes arising from using different gradient geometries: for identical sample lengths and diameters, an x gradient will yield faster-decaying peaks than its z counterpart due to the smaller wiggles originating from the FT of its semicircular profile; higher-order z^n gradients will be associated with "lifted" baselines due to the slow variation of resonance frequencies around the origin; imaginary components will be associated with even-powered z^n gradients due to their lower symmetry when viewed as a function of sample position.

Supporting Information Available: Quicktime animations of magnetization vectors excited throughout a constant-time-based encoding sequence (such as that illustrated in Figure 6A), as well as of the subsequent acquisition processes, were computed by numerical solutions of the Bloch equations using a Matlab-based custom-written program. Compressed versions of these movies were calculated for different chemical shifts (PDF and AVI). This material is available free of charge via the Internet at http://pubs.acs.org.

JA0350785